https://dx.doi.org/10.1016/j.marstruc.2022.103184

Response-based bridge deck limit state considering component-level failure under extreme wave

Deming Zhu[1], You Dong[2], Peng Yuan[3,*], and Guoji Xu[4]

Abstract

Coastal bridges are crucial components of transportation systems; however, they are susceptible to increasing failure risk from extreme waves due to climate change scenarios. Previously, most of the studies focused on the extreme wave forces on the bridge superstructure, while the effects of the overturning moment, bearing constraints, and local damage were seldom discussed. This research conducts an in-depth investigation on the wave-bridge interaction to explore the structural limit state of the coastal bridges subjected to extreme waves considering component failure. Firstly, a three-dimensional (3D) Computational Fluid Dynamics (CFD) model is established and validated to simulate the wave-bridge interaction under various wave scenarios. To lend confidence to the CFD model, laboratory experiments are conducted to improve and validate the simulation results. Subsequently, based on the numerical results, wave force prediction methods are proposed by considering the solitary wave characteristics. Accordingly, the time histories of wave forces are imported into a spatial Finite Element (FE) model of the investigated bridge FE model to compute dynamic structural responses, including bearing reaction forces, bridge displacements, and bearing working states. Then, based on the dynamic structural response, a novel structural limit state incorporating component damage is developed to prevent bearing damages under the wave impacts and corresponding structural demand is parametrically studied and quantified with different wave parameters. Such a study could help optimal and robust designs of coastal bridges and modifications of existing ones.

Keywords: Coastal bridges; Laboratory experiments; 3D numerical models; Overturning effects; Bearing performance; Wave force.

---

[1] Ph.D. student, Department of Civil and Environmental Engineering, The Hong Kong Polytechnic University, Hong Kong; deming.zhu@connect.polyu.hk.

[2] Assistant Professor of Structural Engineering, Department of Civil and Environmental Engineering, The Hong Kong Polytechnic University, Hong Kong; Research Institute for Sustainable Urban Development, The Hong Kong Polytechnic University, Hong Kong; you.dong@polyu.edu.hk.

[3] Postdoctoral Fellow, Department of Civil and Environmental Engineering, The Hong Kong

Polytechnic University, Hung Hom, Kowloon, Hong Kong, peng10.yuan@polyu.edu.hk.
[4] Professor, Department of Bridge Engineering, Southwest Jiaotong University, Chengdu, China, guoji.xu@swjtu.edu.cn; xuguojis@gmail.com.
*Corresponding Author.

1. Introduction

Coastal bridges are vulnerable to extreme waves generated by hurricanes and tsunamis in the climate change scenario. For instance, 81 coastal bridges connecting the Banda Aceh and Malabon were severely destroyed by the 2004 Indian Ocean Tsunami (Unjoh and Endoh 2006). As reported in Padgett et al. (2008), Hurricane Katrina (2005) caused significant damage to the transportation system in the Gulf Coast region, and the overall cost of the repair and reconstruction was estimated at over $1 billion. These repeated disasters punctuate the need to better understand the structural performances of coastal bridges under wave impacts. Additionally, the fast development in bridge systems has continued to occur in coastal communities along with the rapid population growth (Cheng et al. 2018a; Padgett et al. 2012). Moreover, the global climate change effects yield sea level rise and amplification of intensity and frequency of storms (Knutson et al. 2010), which generates increasing risks to the coastal bridges. Therefore, it is valuable to improve our understanding of the wave-bridge interaction mechanisms for the robust and optimize designs of coastal bridges against natural hazards.

Previous studies focusing on wave impacts on the bridge superstructure have led to the first Guide Specification for Bridges Vulnerable to Coastal Storms (AASHTO 2008); however, more relevant research is required to fully comprehend the complex wave-bridge interaction (Fang et al. 2019). For instance, the AASHTO formulas are not suitable for waves with relatively large periods and wavelengths. Specific physical tests or computational models are recommended for an accurate result (AASHTO 2008). There were several studies comparing AASHTO estimation methods with their test results (Azadbakht and Yim 2016; Guo et al. 2015; Seiffert et al. 2015) and bias removal methods (Ataei 2013; G. Xu et al. 2017), but a precise estimation method has not been reached. Additional work is valuable to improve the accuracy of the predictive equations of wave forces on bridge superstructures (Kulicki 2010; Zhu et al. 2021).

On the other hand, most studies focused on the maximum wave force on the deck, while the time series effects during the wave-bridge interaction have attracted attention in recent years. Xu et al. (2018) performed time-domain simulations of wind and wave loads on a three-span suspension bridge and found it challenging to select the combinations of the environmental parameters to be used in the design of the structural component. Ding et al. (2018) investigated the combined earthquake and wave-current effects on bridge piers through experimental tests. Furthermore, the time-series effects of overturning (or rotation) on deck failure has aroused concern in recent years (Cheng et al. 2018a, 2018b; Hayatdavoodi and Ertekin 2015), but the solutions are controversial. For instance, AASHTO (2008) recommended selecting the reference point of the moment at the bottom of the landward girder, while Cai et al. (2018) suggested it at the center of the bent beam. However, Xu (2020) pointed out such a method could underestimate the effects of horizontal wave force. Therefore, more relative studies are required to further investigate the uneven load distribution and overturning moment on coastal bridges.

Moreover, the bearing (or constraint) performance under the wave impacts, which plays an important role in the connection between superstructure and substructure, has not been investigated thoroughly. Since the uplift wave forces are opposed to the traditional downward traffic loads, the bearing responses under wave impacts are rather complicated. The significance of investigations on bearings was highlighted in Bradner et al. (2011), which conducted a 1:5 scale laboratory experiment to explore wave impacts on the bridge superstructure and effects of bearing stiffness. In the following studies, there were some simplified numerical models representing bearings by using springs (Xu and Cai 2015), while which could not fully simulate bearing connections under real-bridge conditions. Saeidpour et al. (2018) performed a static analysis to investigate structural responses under anchor bolt constraints, but the results may deviate from practical dynamic conditions. Ataei and Padgett (2015) investigated bridge responses based on a fluid-structure interaction model, but the bearing constraints were not considered. Salem et al. (2014, 2016) conducted field surveys of damaged bridges by Tohuku Tsunami and utilized Applied Element Method to simulate the structural progressive collapse under wave impacts. They also emphasized the significance of a more detailed analysis based on a three-dimensional (3D) model. Thus, it is vital to study the bearing performance during the wave-bridge interaction utilizing a more sufficient (3D) model and this aspect is conducted in this study.

Recognizing all the issues above, an in-depth investigation of the wave-bridge interaction, wave force prediction method, and the limit states considering component damage based on structural responses is conducted using experiments and 3D numerical models in this study. Specifically, a 3D Computational Fluid Dynamics (CFD) model is established to simulate the wave-bridge interaction, which could calculate changing wave profiles, wave-induced forces, overturning moments, and pressure distributions, improving the understandings of the complex hydrodynamic problem. To lend confidence of the established CFD model, laboratory experiments are conducted to improve and validate the simulation results. Based on the numerical results, wave force prediction methods are proposed and discussed by considering the solitary wave characteristics. Moreover, to formulate the limit state of the coastal bridge under the wave impacts, including overturning moments, displacements, and bearing performance, a 3D bridge FE model considering the effects of material properties, structural dimensions, and system damping on the structural responses is built and corresponding structural demand is discussed and quantified with different wave parameters. The numerical models are improved based on our previous work (Zhu et al. 2021) in the following aspects: (a) the new models simulate more structural details as compared with the previous one, including diaphragms and deck overhangs; (b) the bridge superstructure is divided into 6 girder components and 5 deck components, so that the wave-induced forces on each component could be computed; and (c) dynamic structural analyses are performed by importing the time-history wave forces into the FE model. To the best knowledge of the authors, this is the first time that a limit state which considers the component (bearing) damage is proposed for coastal bridges subjected to solitary wave forces by considering the time histories effects of the overturning moment and bearing performance.

The paper is organized as follows. The experimental and numerical methodologies are introduced in section 2. The experimental results, validations for the CFD model, and simulated wave-bridge interactions are presented in section 3. Wave force prediction methods are proposed in section 4. The structural limit states based on dynamic structural response are formulated and discussed in section 5. Conclusions are drawn in section 6.

2. Experimental setups and 3D numerical modeling

Laboratory experiments of a typical bridge model are conducted, and solitary wave-induced forces are measured to validate the built 3D CFD numerical model. Considering that most of the coastal bridges are located in shallow water regions near shorelines (Chen et al. 2009), the shallow water solitary wave model is adopted in this study, which could simulate the tsunami-induced waves well (Seiffert et al. 2014). Since the storm waves are periodic, such a solitary wave model may not be appropriate to represent storm waves (Seiffert 2014). Besides, to further assess the structural limit states under wave force time histories, the spatial FE model of the bridge is established by using the ANSYS Mechanical APDL package.

2.1 Experimental setups

2.1.1 Investigated bridge and wave model

Based on the post-disaster reconnaissance reports on coastal natural hazards, most of the severely damaged bridges were inadequately designed to resist extreme wave loads (Douglass et al. 2004; Robertson et al. 2007; Suppasri et al. 2013). This study selects a typical type of simply supported bridge significantly damaged in previous hazards (Hayatdavoodi et al. 2014a; Li et al. 2020; Padgett et al. 2008), as shown in Fig. 1. The span length is 15.85 m, girder height is 1.37 m, and deck thickness is 0.18 m. Diaphragms are set in the middle and two ends of the span. Pavement overlays are composed of a 0.1 m thick concrete surface and a 0.18 m thick bituminous concrete pavement on the deck. Concrete guardrails are set at the two sides of the deck. The distance between two neighboring girders equals 1.73 m. The clearance calculated from the initial water level to the girder bottom is set as 4 m. The bridge deck under the wave impacts from seaward tends to be overturned around the overturning center (OTC, see Fig. 1). Deck weight and material properties are listed in Table 1.

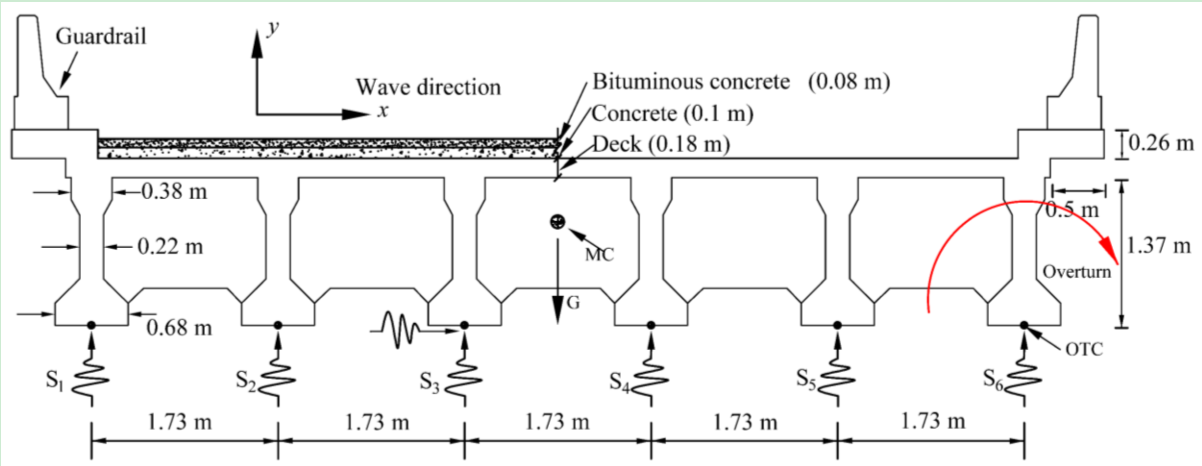

Fig. 1 The schematic diagram of a typical coastal bridge subjected to extreme waves. MC is the mass center of the bridge; OTC is the overturning center; and S_i is bearing connection.

Table 1 Material properties of the investigated bridge model

	Density	Quantity	Weight
Main structure	2.6×10^3 kg/m^3	84.2 m^3	218.9×10^3 kg
Bituminous concrete	2.4×10^3 kg/m^3	$0.08\times8.65\times15.85$ m^3	26.3×10^3 kg
Concrete	2.6×10^3 kg/m^3	$0.1\times8.65\times15.85$ m^3	35.6×10^3 kg
Guardrail	2×10^3 kg/m	15.85 m	31.7×10^3 kg
	Total weight = 312.5×10^3 kg/span = 3,063 kN/span		

The shallow water solitary wave is adopted in this study to simulate the huge waves, which has been frequently used to model some important features of the extreme wave for its stable form and large amplitude (Goring 1978; Yeh et al. 1994). The stable form also benefits measurements at the laboratory and comparisons between experimental and numerical results (Zhu and Dong 2020). The free surface profile η of the solitary wave is as (Miles 1981)

$$\eta(x,t) = H\,\mathrm{sech}^2\sqrt{\frac{3}{4}\frac{H}{D^3}}(x-ct) \tag{1}$$

$$t_0 = \frac{\tanh^{-1}(0.999)}{c\sqrt{\frac{3}{4}\frac{H}{D^3}}} = \frac{3.8}{c\sqrt{\frac{3}{4}\frac{H}{D^3}}} \tag{2}$$

where H = wave height; D = water depth; c = wave celerity; x = coordinate; t = time; and t_0 = the time interval between the wave crest and still water level. In Eq. (1), the wave function η tends to be 0 as t goes infinity, which means the intercept of the leading and trailing edges of the wave t_0 occurs at $\pm\infty$. To meet the wave generating device and numerical analyses, t_0 is defined with a precision expression of three significant figures as Eq. (2) (Goring 1978). Accordingly, the wave period of the solitary wave T equals $2t_0$, and the wavelength λ is calculated as the product of celerity and period.

2.1.2 Experimental setups

A 1:30 scale experiment on the investigated bridge model is conducted in the wave channel at the Hydraulics Laboratory of the Hong Kong Polytechnic University for validation of the 3D CFD model. The wave channel is 30 m long, 1.5 m deep, and 1.5 m wide, with a sidewall made of glass for observation as shown in Fig. 2 (a). Solitary wave is generated by using a piston-type wavemaker at one side of the channel, and a wave attenuation slope is set at the other side to minimize wave reflection effects as Fig. 2 (b). The push panel of the wavemaker is controlled by the DHI's (Danish Hydraulics Institute) control system. The changing water surfaces are measured by three wave gauges around the bridge model. Wave forces on the bridge model in the x, y, and z directions are measured by a multi-axis load cell at a frequency of 100 Hz. Instrument calibrations are performed for all the wave gauges, piston wavemaker, and load cell. A typical photo of the wave-bridge interaction in the test is shown in Fig. 2 (c). The experimental measurements are compared with the CFD numerical results to validate the model. Each case tested is repeated 5 times, and maximum and minimum results and results with a standard deviation larger than ± 5.5% from the mean are removed from the presented results to minimize experimental errors.

The experiment is designed according to the Froude similitude (Chakrabarti 2005). Since the same fluid (i.e., water) is used for both model and prototype, it is hard to achieve exact dynamic similarity for water waves. In the design of the experiment, the effects of surface tension and compressibility are relatively small in this open channel wave flow. The viscosity could also be neglected in this free-surface model when the model is not too small (Briggs

2013). Thus, the Froude similitude is the major scaling criterion in this study. As a result, the Reynolds numbers are inevitably slightly different between the experimental and prototype scales (on the order of $10^4 \sim 10^5$ for the experimental scale and $10^6 \sim 10^7$ for the prototype scale). The authors also examine the effects of the different Reynolds numbers under these two circumstances through different scales of CFD models. It is observed that after conversion, the maximum vertical forces from the 1:30 scale model are no more than 3% larger than those from the prototype model, and the horizontal forces are very close. It means the scale models could provide more conservative results in the engineering field. Nevertheless, additional works on reducing these differences are still encouraged such as adjusting the fluid viscosity in the lab tests. For the Weber number, the surface tension force is negligible as compared with the wave impacts on the bridge, since the latter one could reach over 200 N during the wave-bridge interaction.

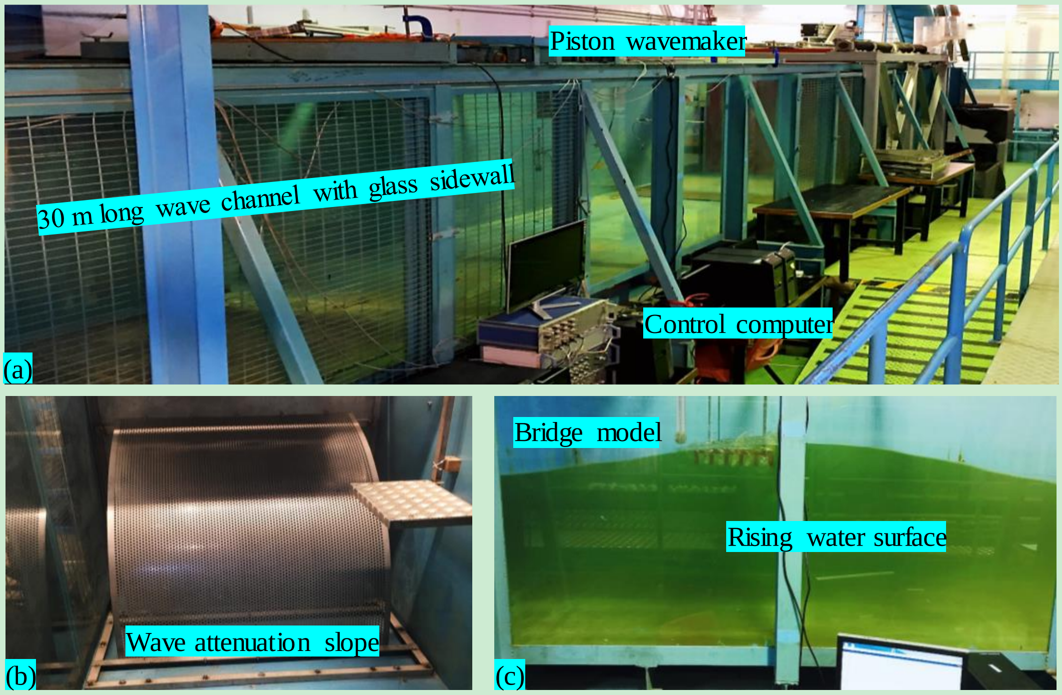

Fig. 2 (a) 30 m long wave channel; (b) wave attenuation slope with meshes; and (c) wave-bridge interaction in the test

2.2 3D Numerical models

2.2.1 CFD modeling and boundary conditions

The fluid motion is simulated using the software ANSYS Fluent, which is improved based on the model in the previous research (Zhu et al. 2021). In this study, the refined model contains more structural details, including diaphragms between the girders and the overhangs at the two sides of the bridge deck (as shown in Fig. 6). Solitary waves are generated from the velocity inlet plane ABCD by using User Defined Functions (UDF), and plane EFGH is set as pressure outlet. The dynamic free surface is prescribed by the Volume of Fluid (VOF) method (Hirt and Nichols 1981) with air set as primary phase and water-fluid set as secondary phase. The whole numerical domain is 140 m long (x direction), 30 m high (y direction), and 20.85 m wide (z direction). The bridge model is located 20 m from the velocity inlet plane, and the distance to the outlet plane is long enough to minimize wave reflection effects. The bridge model is also set as no-slip stationary walls. Wall-layer models were added to produce a smooth distribution along the fluid-wall interfaces following the authors' previous work (Xu et al. 2017). The $y+$ values at the grid cells at the bridge deck surface are around 50 in the established model. The vertical and horizontal wave particle velocities (u and v) are used to generate solitary waves at the velocity inlet plane following Sarpkaya and Isaacson (1981).

In the numerical model, a Boolean subtract is applied for the bridge model. Tetrahedron meshes are utilized to fit the irregular shapes of the girders and diaphragms. To eliminate the influence of the grid on the calculation results, mesh sensitivity analysis is performed, and different fixed time steps are tested to satisfy the Courant Number (Robertsson and Blanch 2020). After several calculations and comparisons of different combinations of mesh sizes and time steps, the mesh size is determined as 0.6 m, the fixed time step is 0.01 s. In addition, the shear stress transport (SST) k-ω model with the turbulence damping factor set as 10 is utilized as the viscous model for the wave-structure interaction. The turbulent intensity of the boundary is set as 2% and the turbulent viscosity ratio is set as 10%. The Pressure-Implicit with Splitting of Operators (PISO) scheme is adopted, and the pressure staggering option (PRESTO) scheme is set for the pressure spatial discretization. The least squares cell-based scheme is used for the gradient discretization, and the second-order upwind is used for momentum advection terms, the spatial discretization of the turbulent kinetic energy, and the specific dissipation rate. Moreover, the stability of the generated solitary wave is also examined that the established CFD model could simulate stable solitary waves with a H/D ratio (wave height/water depth) ranging from 0.15 to 0.45. It should be noted that the effects of added mass, which could be estimated by Morison equations (Gao et al. 2020, 2021; Morison et al. 1950), are relatively small as compared with the impulse force, so that they are neglected in the structural analysis. Also, the allowable structural displacement is relatively small during the wave-bridge interaction due to the large stiffness of the bering constraints between the bridge superstructure and substructure (Xu et al. 2015), so the bridge is assumed as a rigid body in the ANSYS Fluent model, which could also significantly improve the computational efficiency. Detailed information on the established model could be found in Zhu et al. (2021). The 3D numerical model could also be applied to investigate the effects of the bridge substructures on the results by modeling the piers and abutments, which is a critical step to have a deeper understanding of the wave-bridge interaction mechanism (Wei and Dalrymple 2016).

2.2.2 FE modeling of the bridge

The CFD model could simulate the wave-bridge interaction, while the complex bearing reaction, structural deformation, and structural force for the bridge under wave could not be well solved. To investigate structural limit states under the wave impacts, a spatial FE model for the bridge is established by using the ANSYS Mechanical APDL package as shown in Fig. 3. The time-history wave-induced forces from CFD results are imported into the FE model to calculate the dynamic structural responses, including structural displacements and bearing reaction forces.

As indicated in Fig. 3 (a), a full bridge deck with girders and diaphragms is modeled and meshed. All the bearing constraint types are listed in Table 2 with considering practical engineering design (AASHTO 2017; Caltrans 1994). Specifically, all the bearings are set as compression-only in the vertical direction (y direction) since they are usually designed to not allow uplift tension force (Khaleghi et al. 2019). Constraints in the longitudinal direction (z

direction) are assumed at the *R* end for the investigated simply supported bridge model. With respect to constraints in the horizontal direction (*x* direction), only the bearings L3 and R3 are constrained to release the thermal movement at two ends in the horizontal direction (Khaleghi et al. 2019). Only the constrained bearings would produce reaction forces in the corresponding direction under wave forces. A slight difference in the responses of bearings connecting to the same girder at the two ends (e.g., bearing reaction forces on the second pair of bearings $S^2{}_l$ and $S^2{}_r$) could be captured due to the different constraints in the longitudinal direction. It should be noted that to ensure a stable computation after the bearing disengagement occurs, a small tensile stiffness coefficient is assumed for the constraints in the vertical direction, which has little influence on practical results. To accurately extract wave forces from CFD and apply them to the bridge, the deck is divided into 5 deck sections (D1 – D5) and 6 girder sections (G1 – G6) as marked in Fig. 3 (b), and wave forces from the CFD model are import into the FE model as shown in Fig. 3 (c), where $f_{V\text{-}Gi}$ is the vertical force on the girder component; $f_{H\text{-}Gi}$ is the horizontal force on the girder component; $f_{V\text{-}Di}$ is the vertical force on the deck component; and $f_{H\text{-}Di}$ is the horizontal force on the deck component. In this FE model, SOLID 65 and COMBIN 39 are used to simulate the concrete and bearings, respectively. The ultimate concrete compressive strength is set as 37.1 MPa and the axial tensile cracking stress is 3.25 MPa (ACI 2014). The shear transfer coefficient for concrete open and close crack are set as 0.3 and 0.5, respectively, and the Poisson's ratio is taken as 0.167.

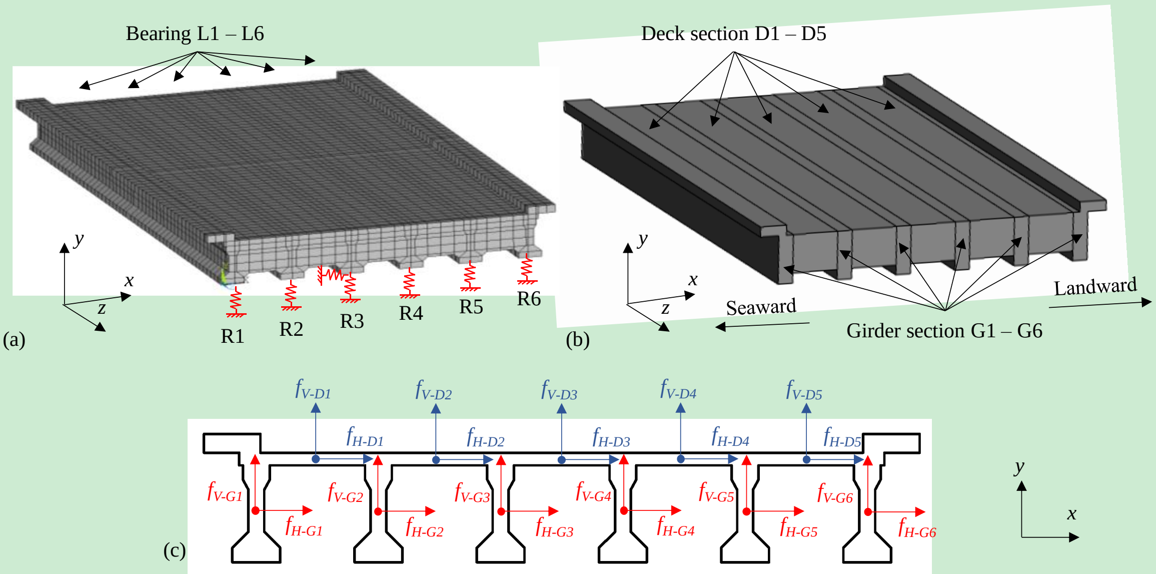

Fig. 3 (a) spatial model of the bridge deck in ANSYS Mechanical APDL; (b) structural segmentation for wave load application; and (c) schematic diagram of the load application method

Table 2 Boundary conditions of the bearings

No.	*x*	*y*	*z*	No.	*x*	*y*	*z*
L1	/	C_O.	/	R1	/	C_O.	Con.
L2	/	C_O.	/	R2	/	C_O.	Con.
L3	Con.	C_O.	/	R3	Con.	C_O.	Con.
L4	/	C_O.	/	R4	/	C_O.	Con.
L5	/	C_O.	/	R5	/	C_O.	Con.
L6	/	C_O.	/	R6	/	C_O.	Con.

Note: / refers to no constraint in the corresponding direction; C_O. refers to compression-only bearing; and Con. refers to constraints in the corresponding direction.

3. Experimental and numerical investigations of wave-bridge interactions

Firstly, experimental validations for the CFD model are presented by comparing the measured wave profiles and wave forces with the numerical results. Then, the validated 3D CFD model is used to simulate the wave-bridge interactions and compute wave force distributions on the bridge for an extensive set of wave conditions. The results of a typical wave case with $D = 14.4$ m, $Z_c = 2.1$ m, and $H = 4.2$ m are presented for illustrative purposes, and time histories of wave-induced forces, overturning moments, and pressure distributions are investigated. Additionally, maximum wave force and overturning moment under different wave scenarios are discussed.

3.1 Measurement-based validation of CFD model

In the experiment, the changing wave profiles under different cases and wave-induced force time histories are measured and compared with numerical results to improve and validate the established CFD model. The generated solitary wave profiles obtained from experimental tests, CFD computations, and analytical solutions (from Eq. (1)) are presented in Fig. 4. Different cases are examined including (a) D = 14.4 m, H = 6 m; (b) D = 15 m, H = 6 m; (c) D = 15.6 m, H = 6 m; and (d) D = 16.2 m, H = 6 m. Note that the 1:30 scale experimental results are converted to prototype scale according to Froude similitude (Chakrabarti 2005). As indicated, Eq. (1) calculates theoretical results with completely symmetrical leading and trailing wave edges, while the water surface could fluctuate at the trailing edge after the wave crest passes, which is observed in both experimental and numerical results. The wave profiles generated by the three methods are well consistent with each other, and the differences at the peak surface elevations are 3% - 6% for all the cases, which are acceptable for the established model (Hayatdavoodi et al. 2014b; Seiffert et al. 2014).

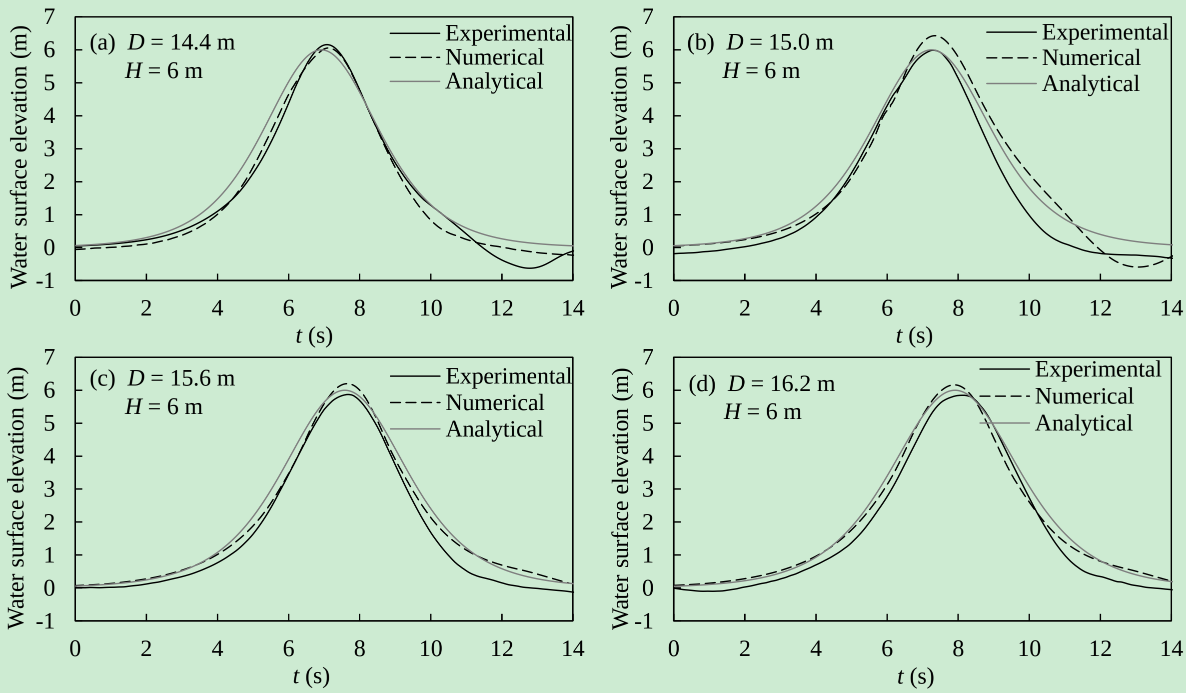

Fig. 4 Comparisons of wave profiles obtained from experimental measurements, CFD models, and analytical function (Eq. (1)) for cases: (a) D = 14.4 m, H = 6 m; (b) D = 15 m, H = 6 m; (c) D = 15.6 m, H = 6 m; and (d) D = 16.2 m, H = 6 m

To further validate the established CFD model, comparisons of the vertical and horizontal wave force time histories (F_V and F_H) between experimental measurements and CFD computations for a typical case with D = 14.4 m, H = 5.4 m are shown in Fig. 5. The vertical wave forces are in close agreement (see Fig. 5 (a)). In Fig. 5 (b), the simulated horizontal wave forces are slightly different from the experimental measurements, which may be caused by the damping effects of the experimental devices even though they are equipped with relatively rigid connections. Overall, good agreement is observed between the computations and laboratory measurements for both the wave profile and wave force time histories, which proves the reliability of the established 3D CFD model.

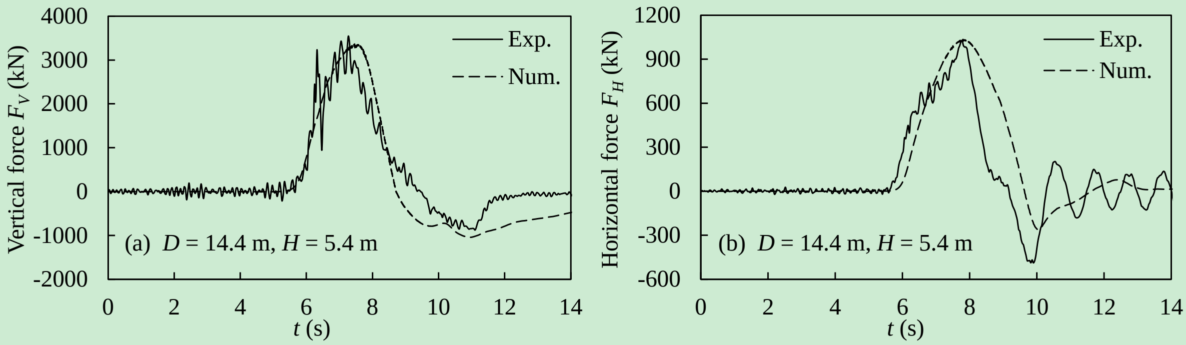

Fig. 5 Comparisons of vertical and horizontal wave force time histories from CFD models and experimental measurements for the case with D = 14.4 m, H = 5.4 m

During the wave-bridge interaction, it is observed that the air could be partially trapped between the rising water level and the bridge structure, while some of it could escape outsides. Such trapped air can increase the total wave loads on the bridge deck, and the partially escaped air would bring uncertainties to the analyses (Bricker and Nakayama 2014). To further explore the contribution of the trapped air on the results, this study compares two scenarios with and without the presence of the trapped air by setting air venting holes on the bridge deck to release the air (Cuomo et al. 2009; Xu et al. 2016). After tests for a wide range of wave excitations, typical results are plotted in Fig. 6. It is observed that through setting air venting holes to release the trapped air, the vertical force $F_{V\text{-MAX}}$ could be reduced by no more than 8%, while the horizontal force $F_{H\text{-MAX}}$ may be enlarged. Such characteristics may be caused by the increase in the contact area between the waves and the bridge in the lateral direction after the escapement of the trapped air. This study mainly focuses on the limit state of the conventional bridge deck (i.e., no air venting holes), which means the effects of the partially escaped air would be less than 8%. Nevertheless, more investigations are encouraged to further quantify the effects of trapped air in the future.

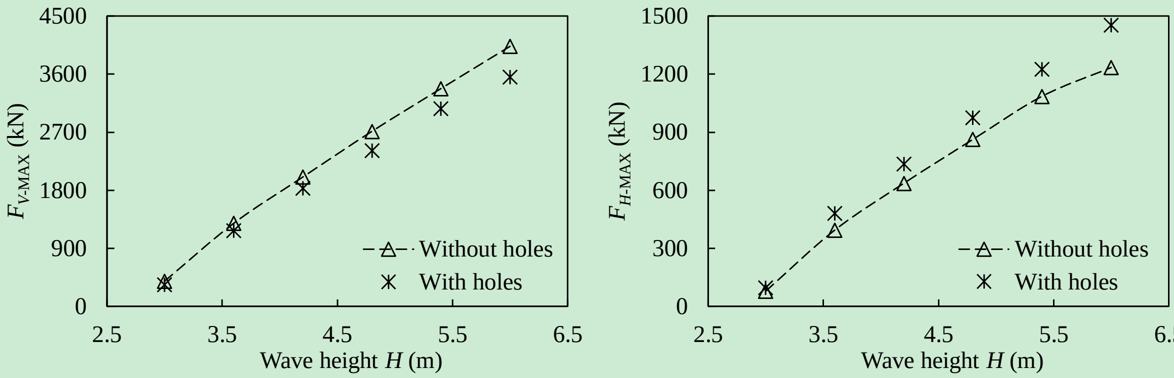

Fig. 6 Comparisons of the maximum veritical and horizontal wave forces ($F_{V\text{-MAX}}$ and $F_{H\text{-MAX}}$) on the bridge deck with and without setting air venting holes for the cases with D = 14.4 m, Z_c = 2.1 m

In addition, this study also compares and examines the effects of freshwater (with a density of 1,000 kg/m^3) and seawater (with a density of 1,025 kg/m^3) on the maximum vertical and horizontal wave forces on the bridge deck ($F_{V\text{-MAX}}$ and $F_{H\text{-MAX}}$), so that the computational results could be applied to real bridges located in coastal regions. As shown in Fig. 7, the wave forces are very close under these two scenarios, and the seawater-induced forces are a bit larger. By comparing multiple datasets of the wave forces, the differences between these two scenarios are no more than 3%, which indicates the established CFD model is applicable for different water conditions.

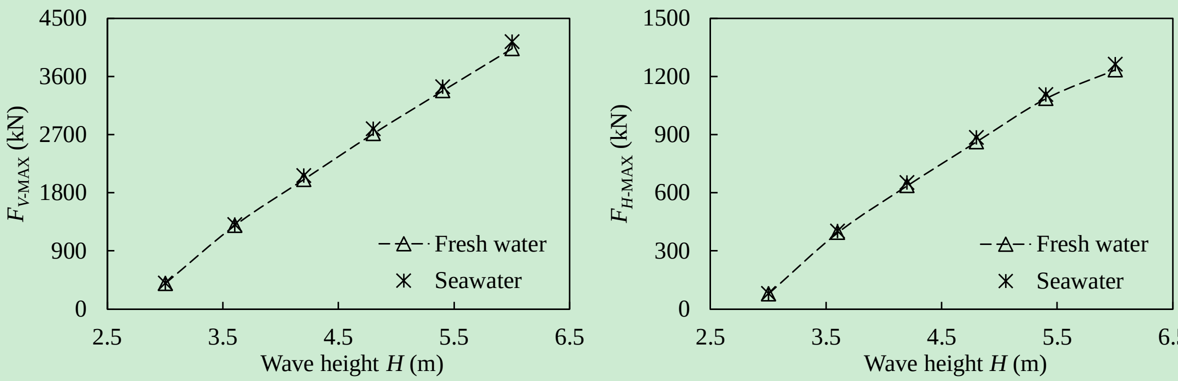

Fig. 7 Effects of fresh water and seawater on the maximum veritical and horizontal wave forces ($F_{V\text{-MAX}}$ and $F_{H\text{-MAX}}$) for the cases with D = 14.4 m, Z_c = 2.1 m

3.2 Wave-bridge interaction in the 3D CFD model

To observe the hydrodynamic wave-bridge interaction, a typical wave case with D = 14.4 m,

Z_c = 2.1 m, and H = 4.2 m is illustrated. In this case, the initial water level is lower than the bridge deck, while the wave is large enough to hit and exceed the deck. Four representative moments of wave profiles and stagnation pressure distributions on the bridge deck are shown in Fig. 8. The fluid phases are represented by different colors based on the VOF method (1 for water phase and 0 for air phase). Lists (ii) and (iii) present stagnation pressure distributions on the deck from the top and bottom views, respectively. When the solitary wave forwards along the x axis and overtopping occurs as shown in Fig. 8 (b), the stagnation pressure on the seaward side of the deck sharply increases, while that on the landward side changes little. The uneven pressure distribution leads to a large overturning moment on the deck, and the deck could be uplifted from the seaward side if the concentrated wave load exceeds the local capacity. Local bearing damages may occur, and structural constraints may be weakened under this condition, threatening structural safety. Fig. 8 (c) indicates the moment when the wave crest has passed the deck. At the trailing edge of the solitary wave, the water surface drops rapidly, resulting in negative pressure beneath the deck (smaller than one atmosphere) as the blue region in Fig. 8 (c). Meanwhile, the deck's upper surface is suffering downward pressure. Hence, there is a momentary downward force on the bridge deck after the uplift slamming as Fig. 5.

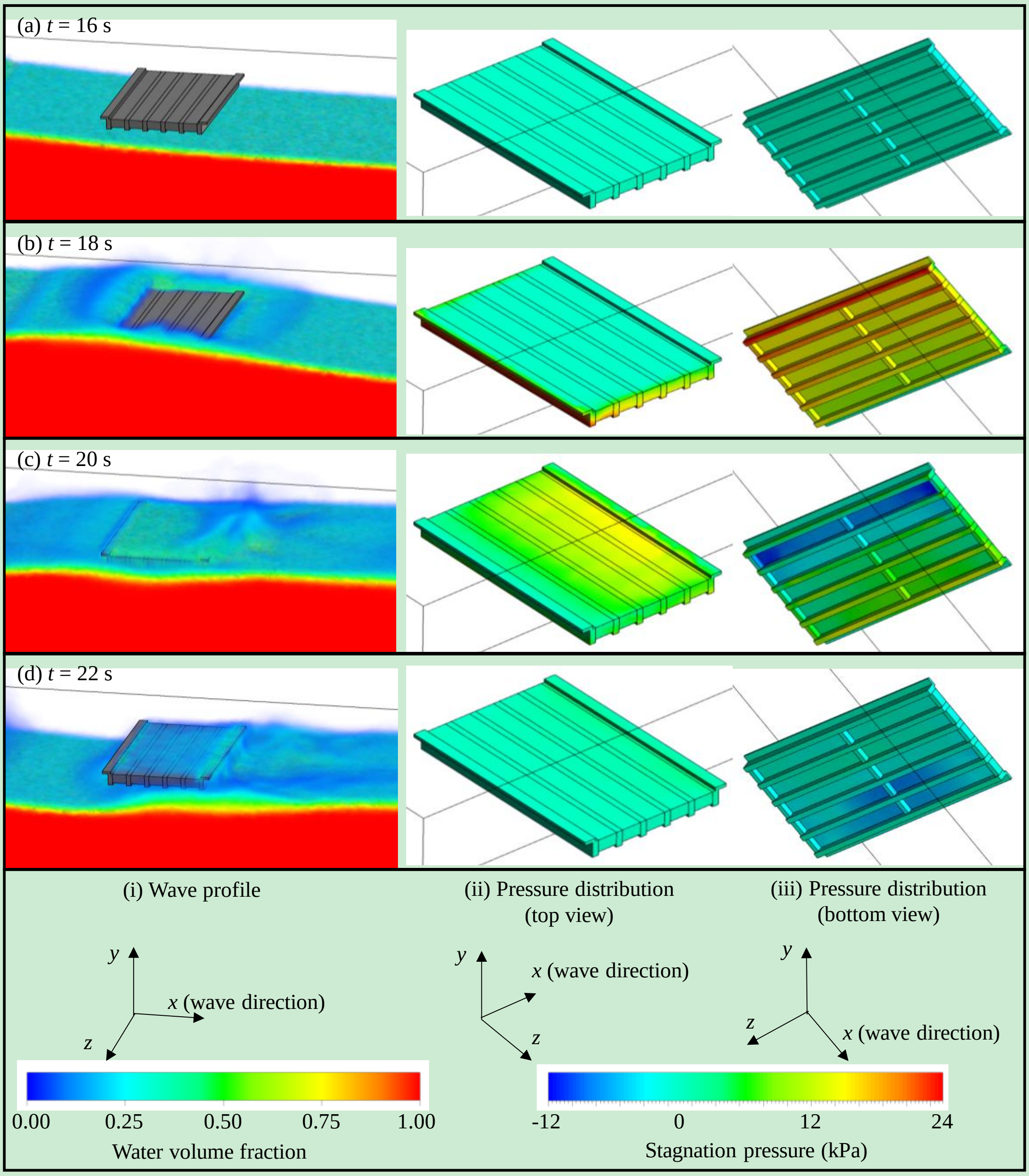

Fig. 8 Wave-bridge interactions and pressure distributions of a typical case with $D = 14.4$ m, $Z_c = 2.1$ m, and $H = 4.2$ m

Wave induced forces on different girder ($f_{V\text{-}Gi}$ for vertical force and $f_{H\text{-}Gi}$ for horizontal force) and deck ($f_{V\text{-}Di}$ for vertical force and $f_{H\text{-}Di}$; for horizontal force) sections (as shown in Fig. 4 (b)) are plotted in Fig. 9. Fig. 9 (a) shows that maximum values of vertical forces on girder 1 to girder 6 reduce in order. $f_{V\text{-}G1}$ has an extremely large peak value at $t = 18$ s, which is caused by the protruding part of the deck. Similarly, Deck section 1 has the largest vertical force $f_{V\text{-}D1}$ at $t = 18$ s as indicated in Fig. 9 (b), and the peak values of $f_{V\text{-}D1} - f_{V\text{-}D5}$ decrease from seaward to the landward side. Minimum values of $f_{V\text{-}Di}$ occur at around 20 s, which are caused by the partial vacuum area between the deck and girders (as the blue region shown in Fig. 8 (c)). Horizontal forces on the girders are shown in Fig. 9 (c), where $f_{H\text{-}G1}$ and $f_{H\text{-}G6}$ have larger peak values than the other girders, which is also due to the protruding part of the deck. Horizontal wave forces on deck components $f_{H\text{-}Di}$ are relatively small such that they are not plotted here. Figs. 8 and 9 reveal the uneven load distributions on the deck during the wave-bridge interaction and potential local structural damages prior to the whole structural damage. The obtained results will be used to predict the wave force extremum and imported into the FE model to investigate the limit state of the bridge in the following sections.

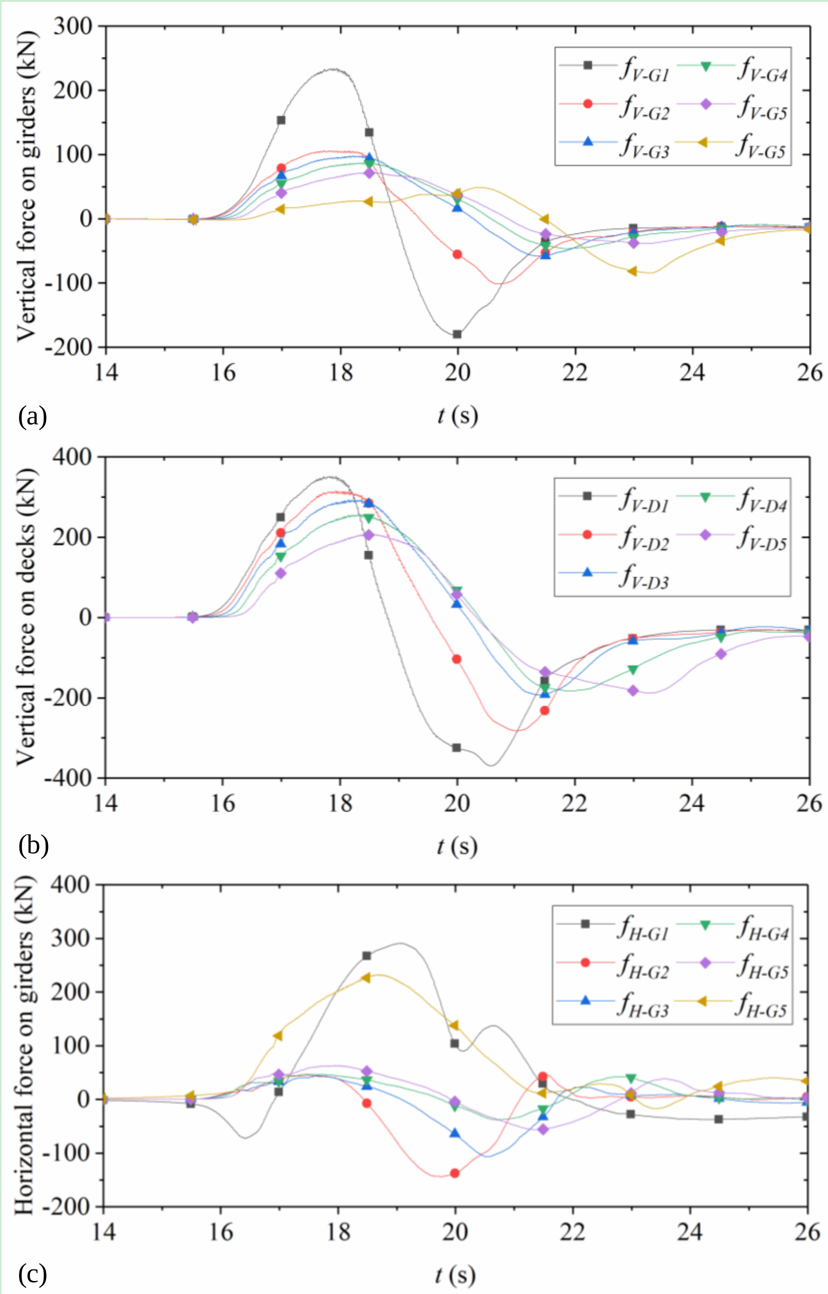

Fig. 9 Time histories results of the case with D = 14.4 m, Z_c = 2.1 m, and H = 4.2 m: (a) vertical wave forces on 6 girder sections $f_{V\text{-}Gi}$; (b) vertical wave forces on 5 deck sections $f_{V\text{-}Di}$; and (c) horizontal wave forces on 6 girder sections $f_{H\text{-}Gi}$

3.3 Maximum wave force and overturning moment

By tracking the time histories of wave-induced forces and overturning moments, the maximum values of vertical force ($F_{V\text{-MAX}}$), horizontal forces ($F_{H\text{-MAX}}$), and overturning moments (M_{MAX}) occur almost simultaneously. Representative results under different inundation and wave conditions are presented in Fig. 10. For unsubmerged scenarios shown in Figs. 10 (a), (c), and (e), $F_{V\text{-MAX}}$, $F_{H\text{-MAX}}$, and M_{MAX} become larger as wave height H increases. $F_{V\text{-MAX}}$ increases with smaller clearance Z_c, while $F_{H\text{-MAX}}$ remains nearly constant except for H = 3.0 m. Figs. 10 (b), (d), and (f) show the results for submerged conditions. Different characteristics are observed that $F_{V\text{-MAX}}$ significantly reduces for larger inundation depth (smaller Z_c) but changes little with H. Both $F_{V\text{-MAX}}$ and $F_{H\text{-MAX}}$ have larger values as Z_c increases in submerged cases. M_{MAX} changes closely with $F_{V\text{-MAX}}$, which means the vertical wave force contributes more to the overturning moment.

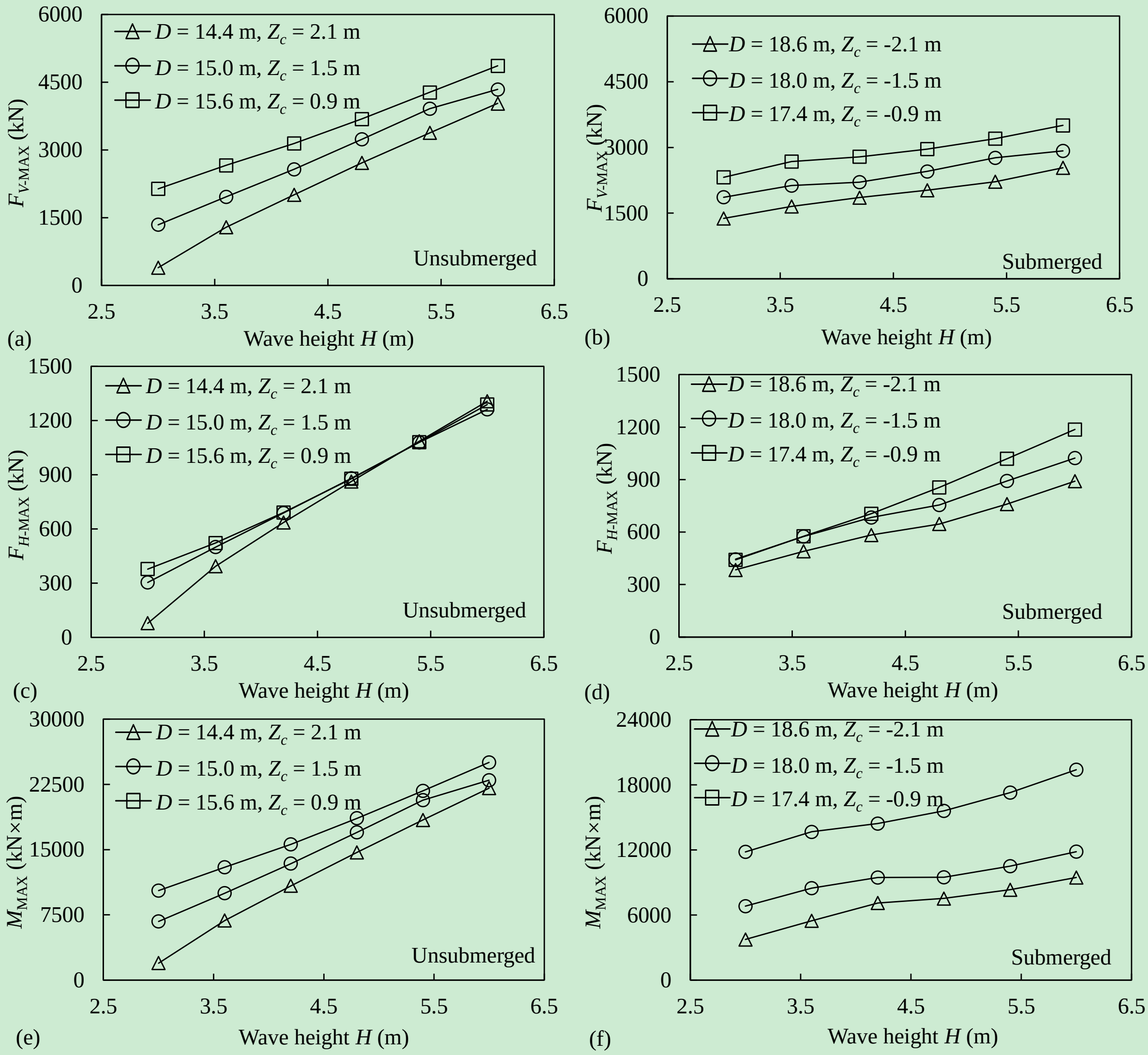

Fig. 10 Maximum wave forces and overturning moments under different inundation and wave conditions

4. Prediction method of wave force extremum

Based on the numerical results above, the prediction methods of wave force extremums are achieved by modifying coefficients of the AASHTO estimation formulas (AASHTO 2008). The AASHTO methods are proposed based on the tests of periodic waves, so the characteristics of solitary waves need to be considered when quantifying solitary wave results. For instance, a soliton has an infinite wave period and wavelength theoretically. Although Goring's method (Goring 1978) is used to estimate the period and wavelength in the tests, the calculated results are still large as compared with those of periodic waves, especially for the long distance at the leading and trailing edges. Hence, this study modifies several parameters of this method to fit the solitary wave results. In AASHTO 2008, the maximum vertical and horizontal wave forces ($F_{V\text{-MAX}}$ and $F_{H\text{-MAX}}$) can be calculated as:

$$\begin{aligned} F_{V-\mathrm{MAX}} &= F_{VS} + F_s = \gamma_w \overline{W} \beta \left(-1.3\frac{H}{D}+1.8\right)\left[1.35+0.35\tanh\left(1.2T-8.5\right)\right] \\ &\left(b_0 + b_1 x_v + \frac{b_2}{y_v} + b_3 x_v^{\,2} + \frac{b_4}{y_v^{\,2}} + \frac{b_5 x_v}{y_v} + b_6 x_v^{\,3}\right)\left(TAF\right) + A\gamma_w H^2 \left(\frac{H}{\lambda}\right)^B \end{aligned} \tag{3}$$

$$\overline{W} = \left[\lambda - \left(\frac{\lambda}{H}\right)\left(Z_c + \frac{H}{2}\right)\right] \tag{4}$$

$$x_v = \frac{H}{\lambda}, \text{ and } \; y_v = \frac{\overline{W}}{\lambda} \tag{5}$$

$$A = \begin{cases} 0.0149\left(\dfrac{Z_c}{\eta_{\max}}\right) + 0.0316 & \text{if } \dfrac{Z_c}{\eta_{\max}} \geq 0 \\ \left[-1562.9 + 1594.5 e^{-\left(\frac{Z_c}{\eta_{\max}}\right)}\right]^{-1} & \text{if } \dfrac{Z_c}{\eta_{\max}} < 0 \end{cases} \tag{6}$$

$$B = 0.6538\left(\frac{Z_c}{\eta_{\max}}\right)^2 + 0.5368\left(\frac{Z_c}{\eta_{\max}}\right) - 1.193 \tag{7}$$

$$\begin{aligned} F_{H-\mathrm{MAX}} &= \gamma_w H^2 \left[a_0 + a_1\left(x_h\right) + a_2\left(x_h\right)^2 + a_3\left(x_h\right)^3 + a_4\left(x_h\right)^4 + a_5\left(x_h\right)^5 + a_6 \ln\left(y_h\right)\right] \\ &\left[a_7 + a_8\left(\frac{W}{\lambda}\right)\right] \end{aligned} \tag{8}$$

$$x_h = \left(\frac{\eta_{\max} - Z_c}{d_b + r}\right) \text{ and } \; y_h = \frac{H}{\lambda} \tag{9}$$

where γ_w = unit weight of water; TAF = the trapped air factor; r = rail height; d_b = the sum of girder height and deck thickness; W = horizontal projection of overhang; and other coefficients could be calculated from the guide specifications (AASHTO 2008).

4.1 Maximum vertical force prediction

To account for the solitary wave characteristics and get an accurate prediction of $F_{V\text{-MAX}}$, the authors examine and compare several methods, including taking the effective section of the solitary wave, adjusting the wavelength and wave height parameters, and adopting the correction coefficient. The coefficient of determination R^2 and the root-mean-square error RMSE are utilized to examine the goodness of the fitting results. After several calculations and comparisons, concepts of effective period T_e and effective wavelength λ_e (as shown in Fig. 11 (a)) are proposed to help predict the maximum wave forces. T_e and λ_e are defined as the period when the water surface elevation is larger than the effective wave height H_e. Such a method could better describe the characteristics of the solitary wave crest since that is where the solitary wave energy mostly concentrates (Longuet-Higgins 1974). The effective wave height H_e is calculated from the wave height H and effective coefficient ε as indicated in Eq. 10, and the relevant period and wavelength (T_e and λ_e) can be further determined from the wave profiles (Longuet-Higgins 1974).

$$H_e = \varepsilon H \tag{10}$$

Sensitivity analyses are performed to determine the value of ε, and the results are listed in Table 3. By comparing R^2 and RMSE values, it is identified that the best predicting performance occurs when $\varepsilon = 40\%$, and the R^2 and RMSE are 0.9607 and 359.16, respectively. The corresponding T_e and λ_e can be calculated from the solitary wave profiles. Replacing T with T_e and λ with λ_e as Eqs. (11) - (13) could get more accurate $F_{V\text{-MAX}}$ for solitary waves.

$$\begin{aligned} F_{V-\mathrm{MAX}} &= F_{VS} + F_s = \gamma_w \overline{W} \beta \left(-1.3\frac{H}{D} + 1.8\right)\left[1.35 + 0.35\tanh\left(1.2T_e - 8.5\right)\right] \\ &\left(b_0 + b_1 x_v + \frac{b_2}{y_v} + b_3 x_v^2 + \frac{b_4}{y_v^2} + \frac{b_5 x_v}{y_v} + b_6 x_v^3\right)(TAF) + A\gamma_w H^2 \left(\frac{H}{\lambda_e}\right)^B \end{aligned} \tag{11}$$

$$\overline{W} = \left[\lambda_e - \left(\frac{\lambda_e}{H}\right)\left(Z_c + \frac{H}{2}\right)\right] \tag{12}$$

$$x_v = \frac{H}{\lambda_e}, \text{ and } \; y_v = \frac{\overline{W}}{\lambda_e} \tag{13}$$

Table 3 R^2 and RMSE values for different ε scenarios

ε	25%	30%	35%	**40%**	45%	50%	55%
R^2	0.8084	0.8283	0.8977	**0.9607**	0.9405	0.8731	0.8246
RMSE	613.60	522.98	458.65	**359.16**	366.91	414.67	428.45

An illustrative example of the case with D = 14.4 m and H = 4.8 m is presented in Fig. 11 (a). The period calculated from Goring's method equals 15.95 s, and apparently, the leading and trailing edges are very long but with small elevations. Taking T_e = 5.17 s, which is about one-third of the original wave period, could better describe the characteristics of wave crest. Comparisons of the various cases under unsubmerged and submerged conditions are shown in Figs. 11 (b) and (c). The predicted values using the modified method match CFD simulated results well in both situations, which means the proposed prediction method has good performance in estimations of solitary wave forces.

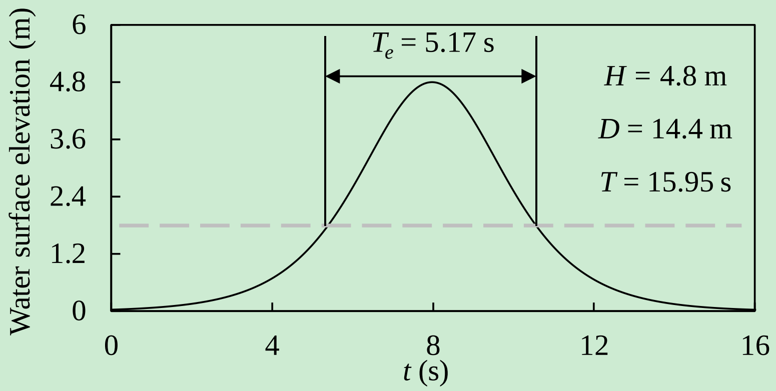

(a) Definition of effective wave period T_e

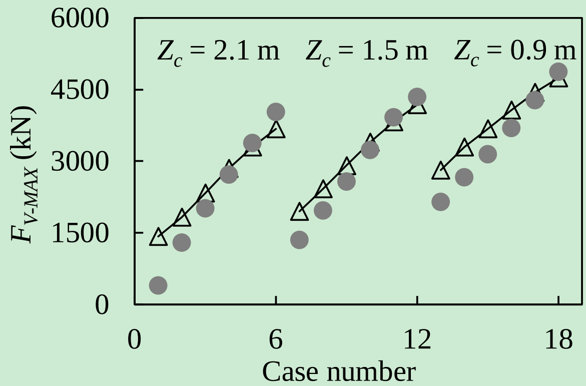

(b) CFD simulated and predicted $F_{V\text{-}MAX}$ under unsubmerged conditions

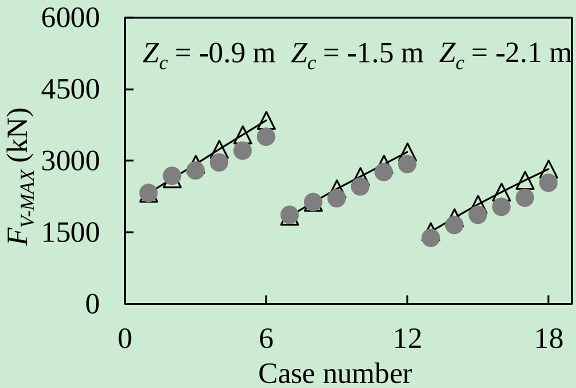

(c) CFD simulated and predicted $F_{V\text{-}MAX}$ under submerged conditions

Note: 6 cases are selected for each clearance (Z_c) with wave height H ranges from 3 m to 6 m. —△— : CFD simulated results and ● : predicted results.

Fig. 11 (a) Definition of effective wave period T_e; (b) comparisons of CFD simulated and predicted $F_{V\text{-MAX}}$ under unsubmerged conditions; and (c) comparisons of CFD simulated and predicted $F_{V\text{-MAX}}$ under submerged conditions

4.2 Maximum horizontal force prediction

In the previous method for periodic waves (AASHTO 2008), the horizontal wave force is calculated by fitting the periodic wave parameters as Eqs. (8) and (9). To better account for the characteristics of the solitary wave crest, the effective period T_e and effective wavelength λ_e are also adopted as Eq. (14). The coefficients x_h and y_h are refitted based on the computed horizontal wave forces using the nonlinear least-squares method (Johnson 2008) as a_1 = 0.26128, a_2 = -0.07207, a_3 = 0.00601, and a_4 = -0.47239. Comparisons of CFD simulated results and predicted $F_{H\text{-MAX}}$ under unsubmerged and submerged conditions are presented in Fig. 12, and good agreements are observed.

$$F_{H-\text{MAX}} = \gamma_w H^2 \left[a_1 (x_h) + a_2 (x_h)^2 + a_3 (x_h)^3 + a_4 (y_h) \right] \tag{14}$$

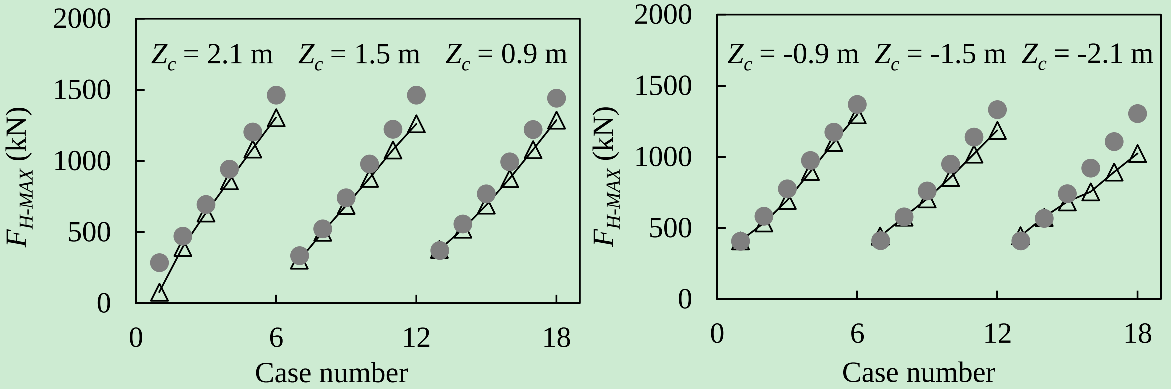

(a) CFD simulated and predicted $F_{H\text{-}MAX}$ under unsubmerged conditions

(b) CFD simulated and predicted $F_{H\text{-}MAX}$ under submerged conditions

Note: 6 cases are selected for each clearance (Z_c) with wave height H ranges from 3 m to 6 m. —△— : CFD simulated results and ● : predicted results.

Fig. 12 Comparisons of $F_{H\text{-MAX}}$ under (a) unsubmerged conditions and (b) submerged conditions

5. Structural limit states considering component failure

Using obtained wave force histories, structural responses under different wave scenarios are calculated to evaluate the bearing performance and structural limit states. A component-level damage evaluation method is formulated and discussed.

5.1 Dynamic structural responses

By collecting wave force histories on each component calculated from the CFD model and applying them to the spatial FE model at corresponding positions of the bridge deck, the displacement of the deck, bearing reaction forces, and bearing working states can be calculated. A typical case with D = 15 m, Z_c = 1.5 m, and H = 4.2 m is selected for illustration purposes. The origin of time t is taken when the wave starts to interact with the bridge to save computational time in the FE analysis (i.e., the period when the water surface rises but has not reached the bridge is not considered). The displacement of the deck at representative moments are presented in Fig. 13. The scale factor is 156.76. At the initial stage before the wave arrives

(t = 1.5 s as shown in Fig. 13 (a)), the middle section of the deck sags naturally due to the gravity, while the two ends are supported by the bearings. When the wave arrives at t = 3 s, the downward displacement is reduced by the vertical wave force. Fig. 13 (c) shows the moment when the bridge is partially uplifted by the wave, and bearings L1 – L3 and R1 – R3 are disengaged (damaged) at this stage. It is observed that the displacement and damage state of each bearing is different under the wave impacts, and the local damaged bearings could influence structural safety. Thus, it is necessary to perform structural analysis to explore the bearing damage and the associated structural limit states.

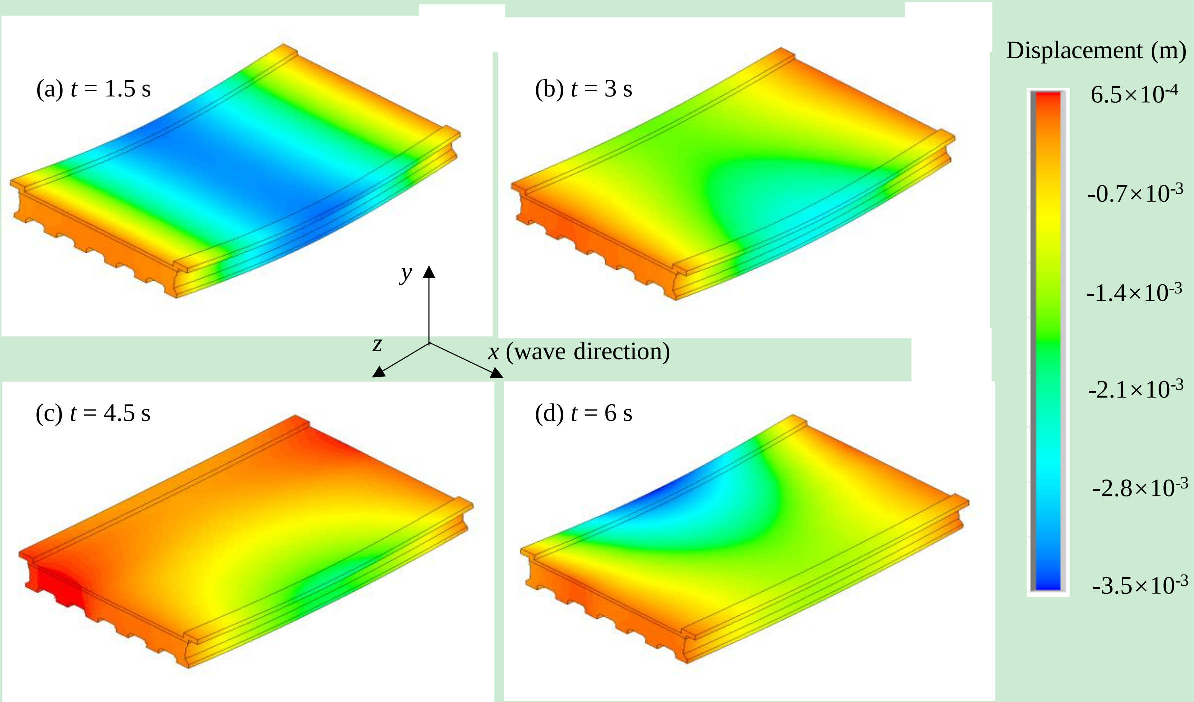

Fig. 13 Displacement of the deck at different moments for a typical case with D = 15 m, Z_c = 1.5 m, and H = 4.2 m

Time histories of bearing reaction forces are shown in Fig. 14. The bearing reaction forces on two ends of the deck (L and R ends) change similarly, so only the results on one end (R end) are shown. In Fig. 14, positive values represent compressed (normal) bearing working states. The "damage" of the bearings herein refers to the disengagement of the bearings caused by the uplift wave impacts, which is often not allowed for the bridge safety (Caltrans 1994; Khaleghi et al. 2019). During the wave-bridge interaction process, reaction forces of bearings R1, R2, and R3 become zero (damaged) at about 4 s successively, since the huge wave comes from the seaward side. Due to the concentrated wave load and extreme overturning moment, local bearing constraints could be destroyed (i.e., reaction force becomes 0 and disengages). Such a local component-level (bearing) damage could occur before the overall failure of the structure (total wave force exceeds the sum of deck weight and connection strength). Hence, identification of the limit states concerning the bearing damages and calculation of the threshold value targeting the phenomenon is necessary.

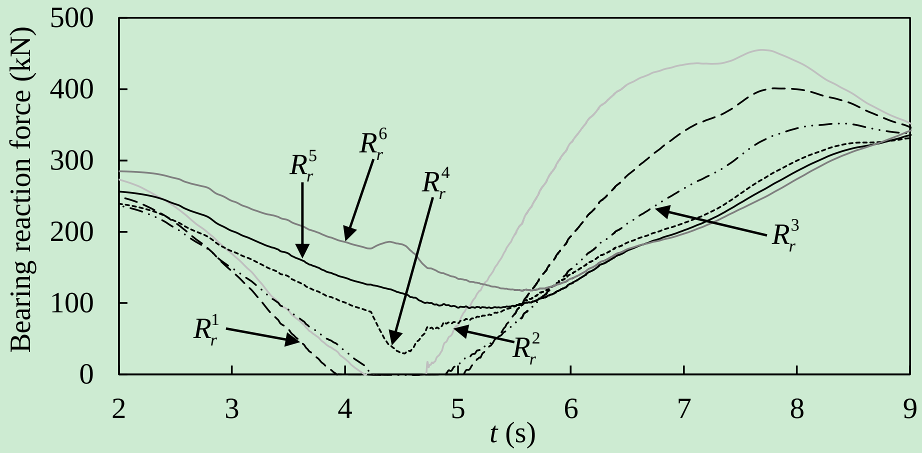

Fig. 14 Time histories of bearing reaction forces for a typical case with D = 15 m, Z_c = 1.5 m, and H = 4.2 m

5.2 Bridge limit state C_{Limit} considering component damage

By tracing the dynamic structural responses under wave forces, it is identified that the extreme wave force and overturning moment can destroy seaward bearings and overturn the bridge deck. Note that this research focuses on the limit state of overturning effect, that is the phase when the structural (bearing) disengagement occurs, but the whole bridge has not been overturned by the waves, and hence the overturning center of the bridge deck OTC is selected at the bottom of the girder 6 based on the computational results (as Fig. 1). The force schematic diagram of the bridge is also plotted in Fig. 1. The deck tends to be uplifted at the seaward side and rotate around OTC. To address this issue, the novel limit state of a coastal bridge subjected to overturning effects from the waves is formulated in this section.

To calculate the limit state preventing bearing damages, some definitions are clarified first as follows. The total deck capacity against overturning effect C_M is mainly contributed by the static weight of the main structure, bituminous concrete, guard rail, etc., and vertical constraints from the connections between the bridge superstructure and substructure if existed. The anti-overturning capacity from the static weight can be calculated as the product of the gravity and the distance from the gravity center to OTC. Hence, the limit state C_{Limit} can be obtained as:

$$C_{\text{Limit}} = \xi C_M = \xi \left(mg \times 2.5L + C_c \right) \tag{15}$$

where ξ = the safety coefficient associated with overturning moment; L = the distance between two neighboring bearings (see Fig. 1); and C_c = the capacity provided from connections, which equals 0 since the constraints are assumed to provide no tension force in this study. Substituting $\xi = 1$, $m = 312.5\times10^3$ kg, and L =1.73 m, C_{Limit} is calculated as 13,704 kN×m. The value of ξ will be further discussed in the following content.

The bearing reaction forces reduce under the effects of horizontal/uplift wave forces, and the residual resistance from the bearings R_M can be calculated by accumulating the product of reaction forces and corresponding force arms of each bearing as:

$$R_M = \sum_{i=1}^{6} \left(R_l^i(t) + R_r^i(t) \right) \times (i-1)L \tag{16}$$

where $R^i_l(t)$ and $R^i_r(t)$ = structural reaction forces of the ith girder on the left and right ends of the deck; and t = time. Similarly, positive values of $R^i_{l(t)}$ and $R^i_{r(t)}$ represent a compressed state of the bearing. Thus, the structural demand associated with the overturning effect caused by the waves D_M can be calculated as

$$D_M = C_M - R_M \tag{17}$$

It should be noted that the overturning-moment-associated structural demand D_M is different from the overturning moment M calculated by accumulating the wave force distributions on the superstructure. The latter one is a measurement of external excitation from wave impacts, while the former one is the structural response which comprehensively considers the effects of structural properties and bearing constraints. Most of the previous studies focused on the investigations of M (AASHTO 2008; G. Xu et al. 2016; Zhao et al. 2020), and this paper explores the influences of D_M for the first time.

Furthermore, when $\xi = 1$, once the R_M becomes zero or $D_M \geq C_M$, it means all the bearings are disengaged and no longer provide any constraint, and the bridge could be washed away. However, a positive R_M cannot ensure a safe state for all the bearings, since uneven wave force distribution on the deck could damage several local bearings as discussed in section 5.1 (See Fig. 14). For instance, a typical time series of the structural demand D_M is plotted in Fig. 15. In this case, water depth D = 14.4 m, clearance Z_c = 2.1 m, and wave height H = 4.2 m. As the wave uplift force increases, D_M gradually increases, reaching maximum value when $t \approx 4.2$ s ($D_{M\text{-MAX}}$ = 12991 kN×m). Then, the uplift force reduces, and downward wave force occurs. Under the combined effects of horizontal/vertical wave forces and deck weight, D_M reduces to negative and reaches its minimum value at t = 8 s. During this process, bearing disengagement occurs as shown in a detailed diagram Fig. 15 (b). As indicated, disengaged bearing ($S^i{}_l$ and $S^i{}_r$) and corresponding damage states (time and demand) are marked by red points. Since the constraints in the z direction are only set at the R side of the bridge, the limit states of bearings at the two ends are slightly different (e.g., $S^2{}_l$ and $S^2{}_r$; and $S^3{}_l$ and $S^3{}_r$). Although the structural demand D_M is always lower than C_M, the component-level damage (bearing) still occurs, which is dangerous for structural safety. Hence, it is necessary to reserve additional capacity to prevent component (bearing) damages, and the safety coefficient ξ should be adopted to modify the C_M to a threshold value (See Fig. 15).

Based on the numerical results in this study, a safety coefficient ξ of 0.7 is suggested, and the limit state C_{Limit} is calculated as 9593 kN×m from Eq. (14) as plotted with a gray line in Fig. 15. Nevertheless, such a coefficient could be modified for specific cases given other structural conditions and climate and hydrological environments, and more relevant studies are required to examine the threshold value. For instance, a smaller value should be adopted in the design stage in hazard-prone areas to prevent structural damage. In addition, the value of C_{Limit} also depends on C_M. Several methods could be utilized to enhance the overall capacity, including increasing the width and weight of the bridge span, using different types of bearings such as tension-compression bearings, and setting additional constraints between superstructure and substructure.

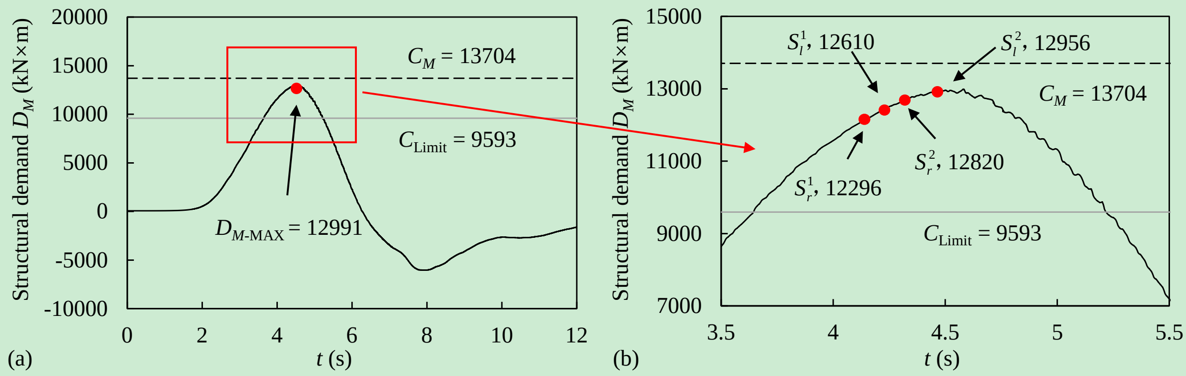

Fig. 15 Time series of bearing resistant R_M and overturning limit state C_{Limit} for the case with D = 14.4 m, Z_c = 2.1 m, and H = 4.2 m. Disengaged bearings and corresponding damage states are marked as by the red points

5.3 Discussion of the structural demand D_M

D_M is the structural demand associated with the overturning moment under wave impacts. Once it reaches the limit state C_{Limit}, the bridge structure and bearing connections are considered at a high failure risk. D_M depends on both the structural characteristics and wave parameters. With respect to the former one, it could be found that D_M is mainly influenced by the bearing properties, including bearing reaction forces $R^i_{l(t)}$ and $R^i_{r(t)}$, the number of bearings i, and the distance between the neighboring bearings L. Hence, to get a smaller value of D_M under a constant wave condition, the bridge should be designed with more bearing constraints and the types and strengths of the bearings should be considered.

To illustrate the effects of wave parameters on the value of D_M, the maximum structural demand $D_{M\text{-MAX}}$ for the investigated bridge model under the different wave and submergence conditions are plotted in Fig. 16. In unsubmerged cases, $D_{M\text{-MAX}}$ increases linearly with the increase of wave height H as indicated in Fig. 16 (a). Also, a larger clearance Z_c could lead to a smaller $D_{M\text{-MAX}}$ under the same wave height H. The wave height H tested under submerged conditions, as shown in Fig. 16 (b), is different from those under unsubmerged conditions to meet the requirement of the H/D ratio. With respect to the Z_c = -0.9 m scenario, the maximum $D_{M\text{-MAX}}$ exceeds C_M when H > 3.5 m because of the extreme wave impact and is not plotted in Fig. 16 (b). Generally, $D_{M\text{-MAX}}$ increases with both wave height H and clearance Z_c, showing different characteristics from submerged conditions.

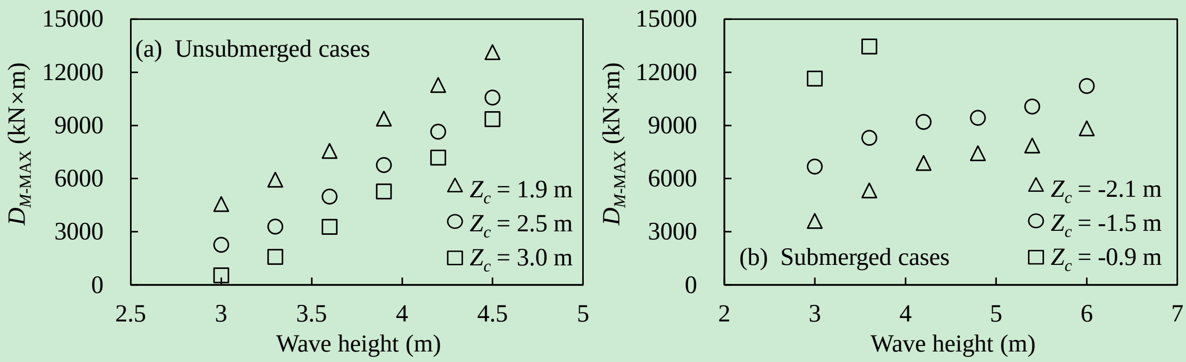

Fig. 16 Maximum structural demand $D_{M\text{-MAX}}$ under (a) unsubmerged and (b) submerged cases

To facilitate the following research and comparisons, the correlations between $D_{M\text{-MAX}}$ and wave parameters are quantified for different submergence scenarios based on the numerical results. After several calculations and comparisons, a second-order polynomial surface model is fitted as

$$D_{M-\mathrm{MAX}} = \alpha_{00} + \alpha_{10} H + \alpha_{01} Z_c + \alpha_{20} H^2 + \alpha_{11} H Z_c + \alpha_{02} Z_c^2 \tag{18}$$

where α_{ij} = fitting coefficients. The fitting results and coefficients are listed in Table 3. The root-mean-square error (RMSE) and goodness of fit (R^2) are adopted to examine the fitting model, and a relatively small RMSE and an R^2 close to 1 prove the convergence of the fitting model (Segura et al. 2019).

Table 3 Fitting coefficients for $R_{M\text{-MIN}}$

	RMSE	R^2	α_{00}	α_{10}	α_{01}	α_{20}	α_{11}	α_{02}
Unsubmerged	312.3	0.983	6438	1211	-7242	573.3	166.8	560.2
Submerged	382.7	0.971	15880	3914	18210	-334.4	-332.7	3490

6. Conclusions

This study conducts an in-depth investigation on the wave-bridge interaction, wave force prediction method, and the limit states considering bearing damages based on structural responses. Laboratory experiments are conducted as a validation method. The time histories of wave-induced force are measured in the laboratory test, which helps to improve and validate the CFD model. 3D dynamic numerical analyses are performed based on the validated CFD and FE models. A novel limit state based on component failures is proposed for coastal bridges subjected to extreme wave forces.

In the light of the results of the numerical and experimental studies on the wave-bridge interaction, it is observed that the extreme wave could induce huge loads concentrated on the seaward side of the bridge. The uneven load distribution on the bridge superstructure leads to a large overturning moment and tends to lift the bridge from one side. The overturning center of the bridge deck OTC is found at the bottom of the landward girder based on the computational results.

By tracing the wave force time series in different cases, the maximum wave-induced forces on the bridge deck are identified and extreme wave force prediction methods are quantified. It is found that maximum wave forces show different characteristics under unsubmerged and submerged conditions. In unsubmerged cases, $F_{V\text{-MAX}}$, $F_{H\text{-MAX}}$, and M_{MAX} become larger as wave height H increases; $F_{V\text{-MAX}}$ increases with smaller clearance Z_c; while $F_{H\text{-MAX}}$ remains nearly constant with a change in Z_c. For submerged conditions, $F_{V\text{-MAX}}$ significantly reduces for larger inundation depth (larger D) but changes little with H; $F_{H\text{-MAX}}$ decreases with larger D; M_{MAX} shows similar trends with $F_{V\text{-MAX}}$. To quantify the maximum wave force, a concept of effective wave period and wavelength (T_e and λ_e) is proposed based on the wave characteristics and estimation formulas are modified accordingly. It is demonstrated that the wave force prediction methods can estimate accurate results for most of the cases.

Based on the numerical results, it is concluded that a local component-level (bearing) damage could occur before the overall failure of the structure (total wave force exceeds the sum of deck weight and connection strength). Hence, identification of the limit state incorporating bearing damages and calculation of the threshold value targeting the phenomenon is of vital importance.

The local bearings could be uplifted under the uneven wave load before the overall wave force exceeding deck weight, which may affect the structural safety. Thus, a safety coefficient ξ is presented to modify the total structural capacity C_M to calculate the new limit state C_{Limit}, which could reserve enough capacity to prevent structural failure and bearing damages. A safety coefficient of 0.7 is suggested based on the investigations in this study and could be modified for specific cases given other structural conditions and climate and hydrological environments.

Furthermore, based on the discussion on the structural demand D_M under various wave parameter scenarios, it is concluded that to improve the structural resistance against the overturning effects, that is to increase the capacity C_M and to decrease the demand D_M, and additional connections against tensile force should be settled for coastal bridges.

In future studies, more investigations are encouraged to quantify the effects of trapped air on the wave impacts and perform sensitivity analyses on the uncertainties in multiple physical parameters. Besides, it is necessary to further explore the effects of bridge substructures (e.g., piers and abutments) and different bridge types, so that the results could be generalized to a range of conditions.

Acknowledgments

The work has been supported by the Research Grant Council of Hong Kong (PolyU 15219819) and a grant PolyU1-BBWM from the Research Institute for Sustainable Urban Development, the Hong Kong Polytechnic University. The opinions and conclusions presented in this paper are those of the authors and do not necessarily reflect the views of the sponsoring organizations.

References

AASHTO. (2008). *Guide specifications for bridges vulnerable to coastal storms*.

AASHTO. (2017). AASHTO LRFD bridge design specifications. *Washington: American Association of State Highway and Transportation Officials*.

ACI Committee 318. (2014). Building Code Requirements for Structural Concrete. *American Concrete Institute*, 524.

ANSYS. (2018). *ANSYS User Manual*. ANSYS INC.

Ataei, N. (2013). *Vulnerability assessment of coastal bridges subjected to hurricane events*.

Ataei, N., & Padgett, J. E. (2015). Influential fluid–structure interaction modelling parameters on the response of bridges vulnerable to coastal storms. *Structure and Infrastructure*

Engineering, *11*(3), 321–333.

Azadbakht, M., & Yim, S. C. (2016). Effect of trapped air on wave forces on coastal bridge superstructures. *Journal of Ocean Engineering and Marine Energy*, *2*(2), 139–158.

Bradner, C., Schumacher, T., Cox, D., & Higgins, C. (2011). Experimental setup for a large-scale bridge superstructure model subjected to waves. *Journal of Waterway, Port, Coastal and Ocean Engineering*, *137*(1), 3–11.

Bricker, J. D., & Nakayama, A. (2014). Contribution of trapped air, deck superelevation, and nearby structures to bridge deck failure during a tsunami. *Journal of Hydraulic Engineering*, *140*(5), 05014002.

Briggs, M. J. (2013). *Basics of physical modeling in coastal and hydraulic engineering*. Coastal and Hydraulics Lab, Engineering Research and Development Center, Vicksburg, MS.

Cai, Y., Agrawal, A., Qu, K., & Tang, H. S. (2018). Numerical Investigation of Connection Forces of a Coastal Bridge Deck Impacted by Solitary Waves. *Journal of Bridge Engineering*, *23*(1), 04017108.

Caltrans. (1994). *Bridge memo to designers. Section 7: Bridge Bearings*. California Department of Transportation Sacramento, CA.

Chakrabarti, S. K. (2005). Physical Modelling of Offshore Structures. In *Handbook of Offshore Engineering* (1001–1054).

Chen, Q., L. Wang, and H. Zhao. 2009. “Hydrodynamic Investigation of Coastal Bridge Collapse During Hurricane Katrina.” *Journal of Hydraulic Engineering*, *135*(3), 175–186.

Cheng, Z., Gao, Z., & Moan, T. (2018a). Hydrodynamic load modeling and analysis of a floating bridge in homogeneous wave conditions. *Marine Structures*, *59*, 122–141.

Cheng, Z., Gao, Z., & Moan, T. (2018b). Wave load effect analysis of a floating bridge in a fjord considering inhomogeneous wave conditions. *Engineering Structures*, *163*, 197–214.

Cuomo, G., Shimosako, K. I., & Takahashi, S. (2009). Wave-in-deck loads on coastal bridges and the role of air. *Coastal Engineering*, *56*(8), 793-809.

Ding, Y., Ma, R., Shi, Y. D., & Li, Z. X. (2018). Underwater shaking table tests on bridge pier under combined earthquake and wave-current action. *Marine Structures*, *58*, 301–320.

Douglass, S. L., Hughes, S. a, Rogers, S., & Chen, Q. (2004). The Impact of Hurricane Ivan on the Coastal Roads of Florida and Alabama: A Preliminary Report. *Rep. to Coastal Transportation Engineering Research and Education Center, Univ. of South Alabama, Mobile, Ala*, 1–19.

Fang, Q., Hong, R., Guo, A., & Li, H. (2019). Experimental Investigation of Wave Forces on Coastal Bridge Decks Subjected to Oblique Wave Attack. *Journal of Bridge Engineering*, *24*(4), 1–10.

Gao, Z., Efthymiou, M., Cheng, L., Zhou, T., Minguez, M., & Zhao, W. (2020). Hydrodynamic damping of a circular cylinder at low KC: experiments and an associated model. *Marine Structures*, *72*, 102777.

Gao, Z., Efthymiou, M., Cheng, L., Zhou, T., Minguez, M., & Zhao, W. (2021). Towards a model of hydrodynamic damping for a circular cylinder with helical strakes at low KC. *Marine Structures*, *78*, 103025.

Goring, D. G. (1978). Tsunamis - the Propagation of Long Waves Onto a Shelf. *Calif Inst Technol W M Keck Lab Hydraul Water Resour Rep KH-R, 38*.

Guo, A., Fang, Q., Bai, X., & Li, H. (2015). Hydrodynamic Experiment of the Wave Force Acting on the Superstructures of Coastal Bridges. *Journal of Bridge Engineering*, *20*(12), 1–11.

Hayatdavoodi, M., & Ertekin, R. C. (2015). Wave forces on a submerged horizontal plate-Part II: Solitary and cnoidal waves. *Journal of Fluids and Structures*, *54*, 580–596.

Hayatdavoodi, M., Seiffert, B., & Ertekin, R. C. (2014). Experiments and computations of solitary-wave forces on a coastal-bridge deck. Part II: Deck with girders. *Coastal Engineering*, *88*, 210–228.

Hirt, C. W., & Nichols, B. D. (1981). Volume of fluid (VOF) method for the dynamics of free boundaries. *Journal of Computational Physics*, *39*(1), 201–225.

Johnson, M. L. (2008). Nonlinear least-squares fitting methods. *Methods in cell biology*, *84*, 781-805.

Khaleghi, B., Warren, L., Fu, Z., Zeldenrust, R., Kestory, E., Stanton, J. F., Mongi, A. N., Walsh, J., Nix, R., & others. (2019). *Experiences in the Performance of Bridge Bearings and Expansion Joints Used for Highway Bridges*.

Knutson, T. R., McBride, J. L., Chan, J., Emanuel, K., Holland, G., Landsea, C., Held, I., Kossin, J. P., Srivastava, A. K., & Sugi, M. (2010). Tropical cyclones and climate change. *Nature Geoscience*, *3*(3), 157–163.

Kulicki, J. M. (2010). Development of the AASHTO guide specifications for bridges vulnerable to coastal storms. *Bridge Maintenance, Safety, Management and Life-Cycle Optimization - Proceedings of the 5th International Conference on Bridge Maintenance, Safety and Management*, 2844–2851.

Li, Y., Dong, Y., & Zhu, D. (2020). Copula-Based Vulnerability Analysis of Civil Infrastructure Subjected to Hurricanes. *Frontiers in Built Environment*, *6*, 170.

Longuet-Higgins, M. S. (1974). On the mass, momentum, energy, and circulation of a solitary wave. *Proceedings of the Royal Society of London. A. Mathematical and Physical Sciences*, *337*(1608), 1-13.

Miles, J. W. (1981). The Korteweg-de Vries equation: A historical essay. *Journal of Fluid Mechanics*, *106*(2), 131–147.

Morison, J. R., Johnson, J. W., & Schaaf, S. A. (1950). The force exerted by surface waves on piles. *Journal of Petroleum Technology*, *2*(05), 149-154.

Padgett, J., Desroches, R., Nielson, B., Yashinsky, M., Kwon, O. S., Burdette, N., & Tavera, E. (2008). Bridge damage and repair costs from Hurricane Katrina. *Journal of Bridge Engineering*, *13*(1), 6–14.

Padgett, J. E., Spiller, A., & Arnold, C. (2012). Statistical analysis of coastal bridge vulnerability based on empirical evidence from Hurricane Katrina. *Structure and Infrastructure Engineering*, *8*(6), 595–605.

Robertson, I. N., Riggs, R. H., Yim, S. C. S., & Young, Y. L. (2007). Lessons from Hurricane Katrina storm surge on bridges and buildings. *Journal of Waterway, Port, Coastal and Ocean Engineering*, *133*(6), 463–483.

Robertsson, J. O. A., & Blanch, J. O. (2020). *Numerical Methods, Finite Difference* (pp. 1–9).

Saeidpour, A., Chorzepa, M. G., Christian, J., & Durham, S. (2018). Parameterized fragility assessment of bridges subjected to hurricane events using metamodels and multiple environmental parameters. *Journal of Infrastructure Systems*, *24*(4).

Salem, H., Mohssen, S., Kosa, K., & Hosoda, A. (2014). Collapse analysis of Utatsu Ohashi bridge damaged by Tohuku Tsunami using applied element method. *Journal of Advanced Concrete Technology*, *12*(10), 388–402.

Salem, H., Mohssen, S., Nishikiori, Y., & Hosoda, A. (2016). Numerical Collapse Analysis of Tsuyagawa Bridge Damaged by Tohoku Tsunami. *Journal of Performance of Constructed Facilities*, *30*(6), 04016065.

Sarpkaya, T., & Isaacson, M. (1981). *Mechanics of wave forces on offshore structures.*

Segura, R. L., Padgett, J. E., & Paultre, P. (2019). Polynomial Response Surface-Based Seismic Fragility Assessment of Concrete Gravity Dams. *12th Canadian Conference on Earthquake Engineering*, *June*, 1–8.

Seiffert, B. R. (2014). *Tsunami and storm wave impacts on coastal bridges*. University of Hawai'i at Manoa

Seiffert, B., Hayatdavoodi, M., & Ertekin, R. C. (2014). Experiments and computations of solitary-wave forces on a coastal-bridge deck. Part I: Flat plate. *Coastal Engineering*, *88*, 194–209.

Seiffert, B. R., Hayatdavoodi, M., & Ertekin, R. C. (2015). Experiments and calculations of cnoidal wave loads on a coastal-bridge deck with girders. *European Journal of Mechanics-B/Fluids*, *52*, 191–205.

Suppasri, A., Shuto, N., Imamura, F., Koshimura, S., Mas, E., & Yalciner, A. C. (2013). Lessons Learned from the 2011 Great East Japan Tsunami: Performance of Tsunami Countermeasures, Coastal Buildings, and Tsunami Evacuation in Japan. *Pure and Applied Geophysics*, *170*(6–8), 993–1018.

Unjoh, S., & Endoh, K. (2006). Damage investigation and the preliminary analyses of bridge damage caused by the 2004 Indian Ocean tsunami. *Proceedings of the 38th UJNR Joint Panel Meeting*, *38*, 267.

Xu, G. (2020). Discussion of “numerical Investigation of Connection Forces of a Coastal Bridge Deck Impacted by Solitary Waves” by Yalong Cai, A. Agrawal, Ke Qu, and H. S. Tang. *Journal of Bridge Engineering*, *25*(1), 1–2.

Wei, Z., & Dalrymple, R. A. (2016). Numerical study on mitigating tsunami force on bridges by an SPH model. *Journal of Ocean Engineering and Marine Energy*, *2*(3), 365-380.

Xu, G., Cai, C., & Deng, L. (2017). Numerical prediction of solitary wave forces on a typical coastal bridge deck with girders. *Structure and Infrastructure Engineering*, *13*(2), 254–272.

Xu, G., & Cai, C. S. (2015). Wave forces on Biloxi Bay Bridge decks with inclinations under solitary waves. *Journal of Performance of Constructed Facilities*, *29*(6), 4014150.

Xu, G., Cai, C. S., Hu, P., & Dong, Z. (2016). Component Level–Based Assessment of the Solitary Wave Forces on a Typical Coastal Bridge Deck and the Countermeasure of Air Venting Holes. *Practice Periodical on Structural Design and Construction*, *21*(4), 04016012.

Xu, Y., Øiseth, O., & Moan, T. (2018). Time domain simulations of wind- and wave-induced load effects on a three-span suspension bridge with two floating pylons. *Marine Structures*, *58*, 434–452.

Yeh, H., Liu, P., Briggs, M., & Synolakis, C. (1994). Propagation and amplification of tsunamis at coastal boundaries. *Nature*, *372*(6504), 353–355.

Zhao, E., Sun, J., Tang, Y., Mu, L., & Jiang, H. (2020). Numerical investigation of tsunami wave impacts on different coastal bridge decks using immersed boundary method. *Ocean Engineering*, *201*.

Zhu, D., & Dong, Y. (2020). Experimental and 3D numerical investigation of solitary wave forces on coastal bridges. *Ocean Engineering*, *209*, 107499.

Zhu, D., Li, Y., & Dong, Y. (2021). Reliability-based retrofit assessment of coastal bridges subjected to wave forces using 3D CFD simulation and metamodeling. *Civil Engineering and Environmental Systems*, *38*(1), 59–83.

Zhu, D., Yuan, P., & Dong, Y. (2021). Probabilistic performance of coastal bridges under hurricane waves using experimental and 3D numerical investigations. *Engineering Structures*, *242*, 112493.